https://doi.org/10.5194/amt-2022-86
Preprint. Discussion started: 3 May 2022

Atmospheric Measurement Techniques Discussions
Open Access
EGU

Lidar and MMCR applied for the study on cloud boundary detection and the statistical analysis of cloud distribution in Xi'an region

Yun Yuan , Huige Di *, Tao Yang , Yuanyuan Liu , Qimeng Li, Qing Yan, Dengxin Hua*

School of Mechanical and Precision Instrument Engineering, Xi'an University of Technology, Xi'an 710048, China

* Corresponding author: dihuige@xaut.edu.cn, dengxinhua@xaut.edu.cn

Lidar and Ka-band Millimeter-Wave Cloud Radar (MMCR) are powerful equipment to detect the height distribution of cloud boundaries, which can monitor the whole life cycle of cloud layers. In this paper, we employ lidar and MMCR to jointly detect cloud boundaries under different conditions (e.g., single-layer clouds, multilayer clouds, and precipitating clouds). By enhancing the echo signal of lidar @1064nm and combining its SNR, he cloud signal can be accurately extracted from the aerosol signals and background noise. The interference signal is eliminated from the power spectrum of the MMCR by using SNR_{min} and the spectral point continuous threshold, and the quality control of the meteorological signal (echo reflectivity factor) obtained by the inversion is carried out, which improves the detection accuracy of the cloud signal. Based on the advantages and disadvantages of the two devices in detecting cloud boundaries under different conditions, cloud boundary statistical rules are established to analyze the characteristics of cloud boundary changes in Xi'an in 2021. The seasonal variation characteristics of clouds show that the frequency distribution of cloud boundaries in vertical height in spring and summer has a similar variation trend. The normalized cloud amount is the lowest in spring (0.65) and the highest in summer (2.46). The frequency distribution of high-level clouds (at 11~12 km) is the highest in autumn, and the clouds in winter are mainly distributed below 8 km. Furthermore, the cloud boundary frequency distribution results for the whole year of 2021 show that the cloud bottom boundary below 1.5 km is more than 10%, the frequency within the height range of 3.06 km~3.6 km is approximately 3.24%, and the frequency above 8 km is less than 2%. The cloud top boundary frequency distribution has the characteristics of a bimodal distribution. The first narrow peak lies at approximately 1.5~3.1 km, and the second peak appears at 7.5~10.5 km.

Keywords: Cloud detection; cloud boundary; lidar; Ka-band Millimeter-Wave Cloud Radar (MMCR); Frequency distribution; Remote sensing and sensors

1 Introduction

Cloud is a mixture of water droplets or ice crystals suspended in the air at a certain height through condensation or condensation after the water vapor in the atmosphere reaches saturation (Wang et al., 1998; Zhou et al., 2016; Wild et al., 2012; Stephens et al., 2012). Cloud vertical structure information (Thorsen et al., 2013; Lohmann et al., 2017; Stephens et al., 2005; Wang et al., 1995; Nakajima et al., 1991) reflects the thermodynamic and dynamic processes of the atmosphere and participates in the global water cycle through formation, development, movement and dissipation (Wild et al., 2012; Zhang et al., 2012; Zhang et al., 2017; Sherwood et al., 2014). However, the vertical structure distribution of clouds has great temporal and spatial heterogeneity and a high change rate, which leads to great challenges in accurately evaluating the radiation effects of clouds at different cloud types and heights.

Notwithstanding, research on the characteristics of cloud vertical structures has always been an important direction of cloud physics research (Zcab et al., 2019). Cloud boundaries are the main information in the study of cloud vertical structure, mainly referring to the cloud bottom and cloud top boundary, of course including the side boundary. The cloud boundary in this paper mainly refers to the cloud bottom and cloud top boundary. In the case of multilayer clouds, it also includes the boundary information of intermediate discontinuous clouds (Zhou et al., 2019; Varikoden et al., 2011; Li et al.,2013; Ward et al.,2004; Zhang et al., 2018; Kuji et al.,2013; Kitova et al. 2003; Cao et al. 2021). With the development of remote sensing detection technology, MMCR (Görsdorf et al., 2015; Kollias et al., 2017; Kollias et al., 2007) and lidar (Apituley et al., 2000; Motty et al., 2018; Cordoba et al., 2017) are effective instruments for cloud boundary detection.

The common methods of detecting cloud boundaries by lidar include the threshold method and differential zero-crossing method. The threshold method (Kovalev et al., 2005) uses the background signal to measure the amplitude of the echo signal. The first point where the echo signal is higher than the background signal and exceeds the set threshold is the cloud bottom boundary. However, in fact, due to the existence of noise, the point with an obvious increase in amplitude may not be found under the condition of a low signal-to-noise ratio (SNR), so the cloud bottom boundary cannot be judged. The differential zero-crossing method proposed by Pal et al. (Pal et al.,1992) differentiates the echo signal to obtain *dP/dr,* and the zero crossing point from negative to positive is the cloud bottom boundary. The threshold method, differential zero crossing method and variant detection method are all based on feature points of cloud boundaries (Streicher et al., 1995). It is easily affected by noise, and some indicators must be introduced in the specific implementation process to determine the cloud boundary through complex detail debugging, which brings certain difficulties to accurate cloud boundary detection. Young (Young et al., 1995) designed an independent double-window algorithm to detect cloud bottom and top boundaries by combining the lidar signal and a known atmospheric backscatter signal, but the algorithm needs to manually adjust the window size or the selection of the threshold. Based on the WCT (wavelet covariance transform) method, Morille et al. (Morille et al., 2007) determined the local maxima on both sides of the cloud peak as the cloud bottom and cloud top, but the cloud bottom and cloud top detected by this method will be overestimated and underestimated, respectively. Mao Feiyue (Mao et al., 2011) adopted a multiscale hierarchical detection algorithm, selected the starting and ending points of the feature area as the cloud bottom and cloud peak, and realized the detection of cloud top and cloud bottom through multiple iterative updates.

The determination of the cloud boundary by MMCR is mainly based on the threshold of the echo reflectivity factor to detect the cloud boundary (Haper et al., 1966; Hobbs et al.,1985; Platt et al., 1994; Brown et al., 1995). Kollias et al. (Kollias et al., 2007) judged the SNR value of a 5×5 grid centered on a distance library. If the SNR of more than 9 consecutive libraries reaches the threshold, the distance library is a cloud signal; otherwise, it is judged as a noncloud signal. Clothiaux et al. (Clothiaux et al.,1999) used 35 GHz millimeter wave cloud measuring radar to analyze different types of clouds and considered that the dynamic range of the cloud reflectivity factor is -50~20 dBZ. Due to the existence of certain ground object echoes and biological groups (including insects and other biological particles) in the lower atmosphere, it will interfere with the real cloud echo signal (Luke et al.,2008; Görsdorf et al.,2015; Oh et al.,2016; Melnikov et al.,2013; Melnikov et al., 2015). If the subjective reflectivity factor threshold is directly used to determine the cloud signal, it is not suitable for all cloud types. Therefore, when

https://doi.org/10.5194/amt-2022-86
Preprint. Discussion started: 3 May 2022

the cloud signal cannot be accurately identified, it will result in large errors in the detection of cloud boundaries.

Research on the macro- and microscopic structures of clouds in a specific area mainly relies on ground-based observations. At present, for better cloud detection, it is necessary to combine lidar and MMCR to observe and study local clouds (Sauvageot et al.,1996; Intrieri et al., 1993; Wang et al., 2000; Sasse et al., 2001). This study will combine the advantages of lidar and MMCR in detecting clouds to achieve high-precision cloud boundary detection and inversion. We effectively identify cloud signals from the power spectrum data of MMCR, and through data quality control, the interference signal caused by floating debris is eliminated to improve the detection accuracy of the cloud boundary. Based on the idea that the MMCR only presents the cloud signal to make cloud boundary detection simple and easy to operate, in this paper, we effectively separate the cloud signal from aerosol and background noise by enhancing and transforming the lidar signal and combining the SNR (Xie et al., 2017) to realize the accurate detection of cloud boundaries. By analyzing the results of cloud boundary detection by two instruments under special weather conditions in Xi'an, the cloud boundary evaluation criteria for the joint observation of the two instruments are established, and the variation characteristics of cloud boundary height over Xi'an in 2021 are statistically analyzed in detail.

2 Observation and Instrument

Xi'an (107.40 ~ 109.49°E and 33.42 ~ 34.45°N) is located in the Guanzhong Basin in the middle of the Weihe River Basin, bordering the Weihe River and the Loess Plateau to the north and the Qinling Mountains to the south. Xi'an has a semihumid climate. Due to its special geographical location, it is particularly urgent to analyze cloud observations and analyses in Xi'an. The lidar and MMCR are installed at the Jinghe National Meteorological Station in China, placed side by side at a distance of 50 m, and both adopt vertical observation mode to obtain the vertical structure information of sky clouds. Fig. 1 shows the topography of Xi'an and the site location of the Jinghe Meteorological Station.

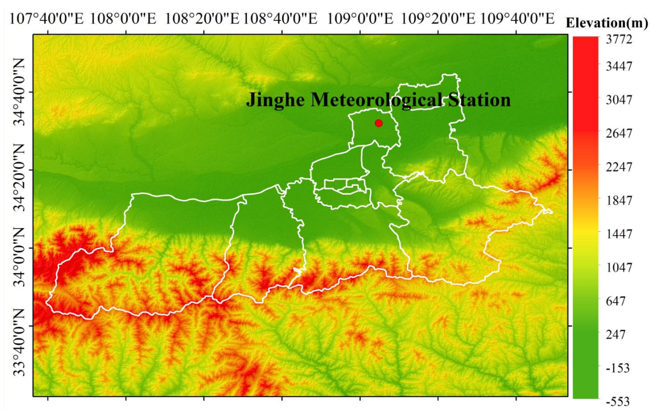

Fig. 1. Geographical coverage of Xi'an (107.40-109.49°E, 33.42-34.45°N). The red dot indicates the location of the Jinghe National Meteorological Station in Xi'an.

The lidar used in this paper was developed by Xi'an University of Technology. The Ka-band Millimeter-Wave Cloud Radar (MMCR) is the HT101 all-solid-state cloud radar researched by Xi'an Huateng Microwave Co., Ltd.

https://doi.org/10.5194/amt-2022-86
Preprint. Discussion started: 3 May 2022

Atmospheric Measurement Techniques Discussions
Open Access
EGU

Its main parameters are shown in Table 1 and Table 2.

Table 1 Main parameters of the lidar

Indicators	Devices	Main parameter
Launch system	Laser	Nd:YAG; 0.75J@1064nm
Receiving system	Cassegrain telescope	Φ400 mm
	Filter	0.5 nm
Detection system	Detector	APD
	Sampling mode	Analog detection
Spatiotemporal resolution	Time resolution	2 mins
	Range resolution	3.75 m
Pulse accumulation		2000

Table 2 Main parameters of MMCR

Indicators		Detailed description
Radar system		All solid-state; All coherent Doppler; Pulse compression
Working frequency		35 GHz, and wavelength is 8.6 mm
Detection altitude range		≥15 km
Detection blind area		150 m
Spatiotemporal resolution	Time resolution	5s
	Range resolution	30 m
Scanning mode		Vertical headspace fixed pointing
Pulse width		$1\mu s$、$5\mu s$、$20\mu s$
Detection accuracy		$Z \le 0.5\ dB$、$V \le 0.5\ m/s$、$W \le 0.5\ m/s$

3 Method

Using active instruments to determine cloud boundaries through remote sensing measurements, echo signals in clear sky areas decay rapidly with increasing detection distance. When the cloud signal is detected, the amplitude of the echo signal begins to increase sharply. Usually, in the actual observation process, the background noise or aerosol layer will also increase the amplitude of the echo signal, but the backscattering intensity of the cloud layer is more continuous and stronger than the aerosol layer and background noise. Therefore, cloud layer and cloud boundary detection can be realized according to the characteristic changes of echo signals.

3.1 Lidar cloud boundary detection

When using lidar for detection, the laser beam propagates in a clear atmosphere, and the received echo power continuously decreases with increasing detection height. However, the beam into the clouds (or aerosols, etc.), the echo power increases suddenly and becomes stronger at a distance above the cloud bottom. The lidar equation owing to elastic backscattering can be written as (Motty et al., 2018),

$$P(\lambda,r)=C\cdot\frac{\Delta r\cdot\beta(\lambda,r)}{r^2}\cdot\exp\left[-2\int_0^r\sigma(\lambda,r')dr'\right]+E(\lambda,r)+N_{bcak}(\lambda,r'') \tag{1}$$

where λ is the wavelength of the emitted light, r represents the detection distance, and C is the system constant, which is determined by the laser energy, the receiving area of the telescope, the quantum efficiency of the detector, etc. Δr is the detection range resolution of the system, and $\beta(\lambda,r)$ and $\sigma(\lambda,r')$ are the atmospheric backscattering coefficient and atmospheric extinction coefficient, respectively. $N_{bcak}(\lambda,r'')$ is the background noise received by the system. $E(\lambda,r)$ represents noise brought to the detection system obtained by calibration.

To avoid amplifying the high-level noise signals, we do not perform the distance square correction Eq. (1) and directly process it as follows:

$$P_{new}(\lambda,r)=\frac{P(\lambda,r)-E(\lambda,r)-N_{bcak}(\lambda,r'')}{C\cdot\Delta r} \tag{2}$$

For ground-based lidar, the echo signal at a certain height range (>15 km in this study) can be considered background and electrical noise, $N_{bcak}(\lambda,r'')$ can be estimated with the signal within this range, and the standard deviation of the noise within the distance range is calculated:

$$Sd=\left[\frac{1}{n-1}\sum_{i=1}^{n}\left(x_i-\frac{1}{n}\sum_{i=1}^{n}x_i\right)\right]^{\frac{1}{2}} \tag{3}$$

where x is the background noise signal. The noise of the lidar signal can be expressed as

$$\mathrm{Noise}(r)=k\cdot Sd \tag{4}$$

After statistical analysis of the system noise, we set k=4 in this paper. Usually, the moving average of $P_{new}(\lambda,r)$ is performed to reduce the influence of random noise. However, the selection of the sliding window directly affects the quality of the signal. Therefore, in this paper, we use the soft-threshold wavelet denoising method to process $P_{new}(\lambda,r)$ to obtain $P_{new\_s}(\lambda,r)$. To avoid atmospheric turbulence and noise interference, $P_{new\_s}(\lambda,r)$ is processed in one step according to the algorithm flow in Fig. 2, and the enhanced signal $P_{new\_sp}(\lambda,r)$ is obtained, as shown in Fig. 3b) and Fig. 4b). The cloud signal is prominently increased from the background noise and the aerosol signal compared to Fig. 3a) and Fig. 4a). In this paper, we consider that the echo signal above 15 km is caused by background and electrical noise. By fitting the echo signal slope in the height range of 15 km~20 km, the slope is used as the base slope to distinguish the cloud layer and aerosol layer (as shown by the magenta line in Fig. 3b and Fig. 4b). Without considering the bottom echo signal (0~2 km), the amplitude of the echo signal received by the lidar will decrease with increasing detection height according to the fitted slope, as shown by the blue line baseline in Figs. 3b) and 4b). When the beam senses the presence of clouds, the amplitude of the echo signal will exceed the blue baseline. The SNR of the echo signal is an important parameter to distinguish the cloud layer and aerosol layer in the echo signal and calculate the SNR of P_{new_sf} with Eq. (5) (Xie et al., 2017),

$$SNR(r,\lambda)=\frac{N\cdot P(r,\lambda)}{\sqrt{N\cdot P(r,\lambda)}+N\cdot P_{back}} \tag{5}$$

where N is the pulse accumulation and P_{back} is the solar background noise power. As shown in Figs. 3c) and 4c), the SNR of the cloud layer is higher than that of the aerosol layer and background noise, and the SNR in the cloud layer is approximately equal to 5 (obtained based on multidata statistical analysis in different situations). Combined with the SNR threshold, the detected cloud information is shown in Figs. 3d) and 4d).

https://doi.org/10.5194/amt-2022-86
Preprint. Discussion started: 3 May 2022

Atmospheric Measurement Techniques Discussions

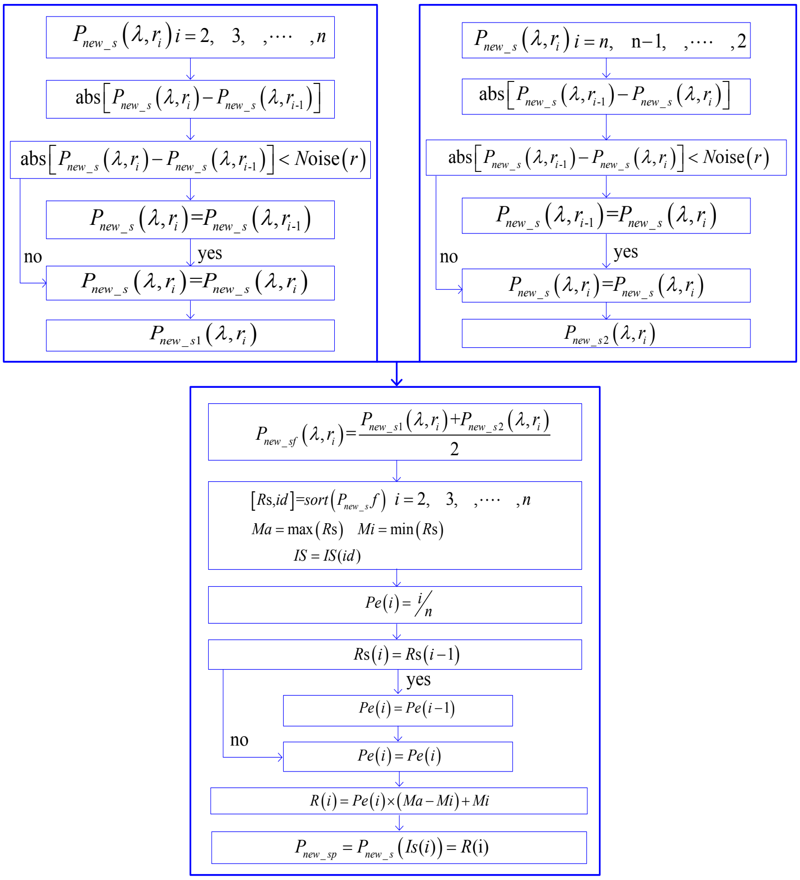

Fig. 2 The P_{new_sp} of the lidar @1064 nm signal processing flow chart

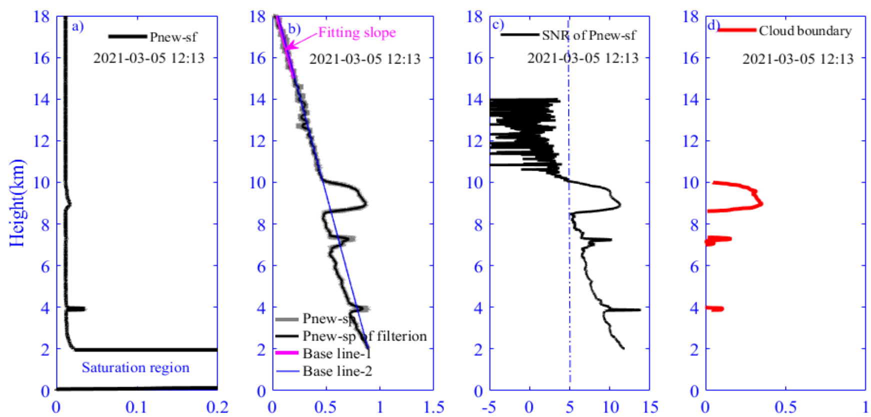

Fig. 3 Detection results of the lidar at 19:15 on March 4, 2021: a) P_{new_sf} of the 1064 nm signal, b) P_{new_sp} of the 1064 nm signal, c) SNR of $P_{new\_sf,}$ and d) cloud information detected

https://doi.org/10.5194/amt-2022-86
Preprint. Discussion started: 3 May 2022

Atmospheric Measurement Techniques Discussions

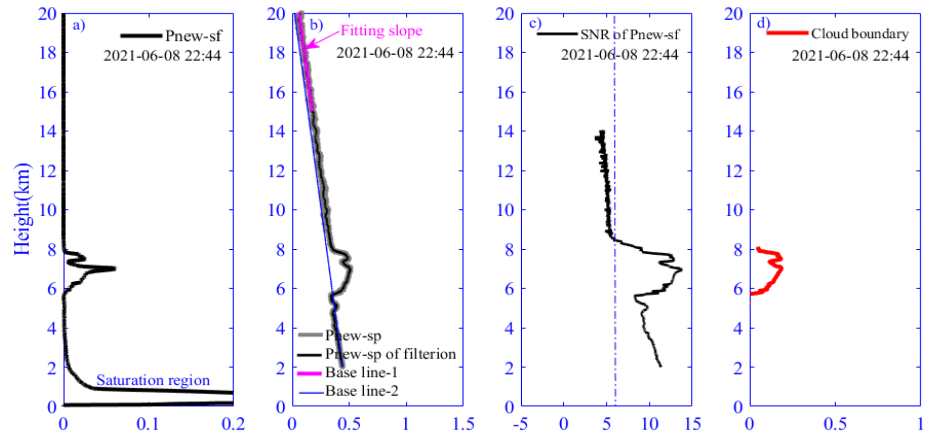

Fig. 4 Detection results of the Lidar at 22:44 on June 8, 2021 a) P_{new_sf} of the 1064 nm signal, b) P_{new_sp} of the 1064 nm signal, c) SNR of P_{new_sf}, d) cloud information detected

3.2 MMCR cloud boundary detection

Identifying cloud signals from power spectrum of the MMCR is affected by the noise level, especially when the SNR is low. As shown in Fig. 5, if all the spectral points above the noise level are integrated, it will bring a large error to the inversion of its characteristic parameters (echo reflectivity, spectral width, radial velocity, etc.). Therefore, it is necessary to carefully identify the cloud signal in the power spectrum signal. When there is a meteorological signal in the power spectrum, the general signal has a certain SNR and the number of spectral points, while the SNR of the noise is very low or the number of continuous spectral points is small, indicating that there is no meteorological signal (Zheng et al., 2014). Accordingly, by calculating the noise and signal boundary, we count the number of continuous spectrum signal points greater than the noise and signal boundary. Set the SNR threshold and the spectral point threshold to evaluate whether each continuous data point is a cloud signal. SNR_{min} refers to the SNR of the smallest measurable cloud signal in the power spectrum. When the signal is greater than SNR_{min}, it is considered to have cloud signal; otherwise, there is only noise signal. Fig. 6 shows the algorithm flow chart of MMCR inversion cloud signal recognition. Referring to the empirical formula proposed by Riddle (Riddle et al., 1989), the SNR_{min} can be calculated by Eq. (6),

$$SNR_{\min}=\frac{25\sqrt{N_F-2.1325+\frac{170}{N_P}}}{N_F\cdot N_P} \qquad (6)$$

where N_F is incoherent accumulation, and N_P is the number of *FFT* (Fast Fourier Transform) sampling points. The N_F and N_P of the MMCR used in this paper are 32 and 256, respectively, and the SNR_{min} is -17.74 dB by calculating the SNR_{min}. Adjust the SNR_{min} according to the measured data of the MMCR, and finally determine the SNR_{min} = -20 dB. Referring to the research results of Shupe et al. (Shupe et al., 2004), N_{ts} is set to 5. When the spectral signal meets the thresholds of SNR_{min} and N_{ts}, it is considered that there is a cloud signal in the power spectrum, and cloud feature parameter calculation is performed, flow of cloud signal recognition algorithm is shown in Fig. 6a.

https://doi.org/10.5194/amt-2022-86
Preprint. Discussion started: 3 May 2022

Atmospheric Measurement Techniques Discussions

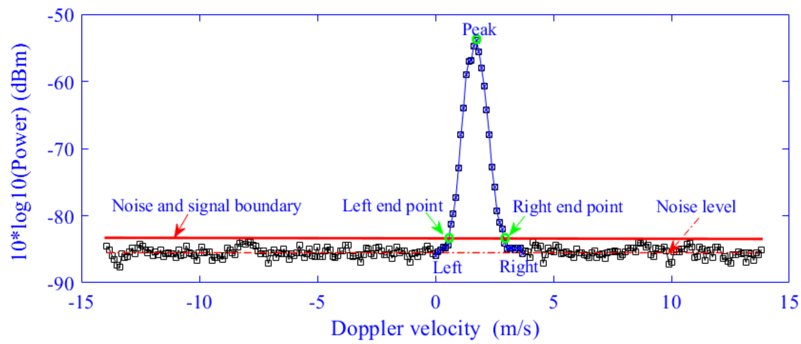

Fig. 5. Schematic diagram of cloud signal recognition in the power spectrum

The echo signals of the floating debris in the bottom atmosphere have the characteristics of a small reflectivity factor, small velocity and large spectral width. To further eliminate interfering wave information, we obtained the data quality control threshold by counting the characteristic changes of planktonic echoes in the boundary layer under cloud-free conditions. As shown in Fig. 6b), when the subjective echo intensity Z<-20 dBZ, the absolute value of radial velocity is less than 0.2, and the velocity spectrum width >0.3 is used as the threshold for removing nonmeteorological information, the expected data quality control requirements can be met. Cloud boundaries are detected using data quality-controlled cloud echo reflectivity factors.

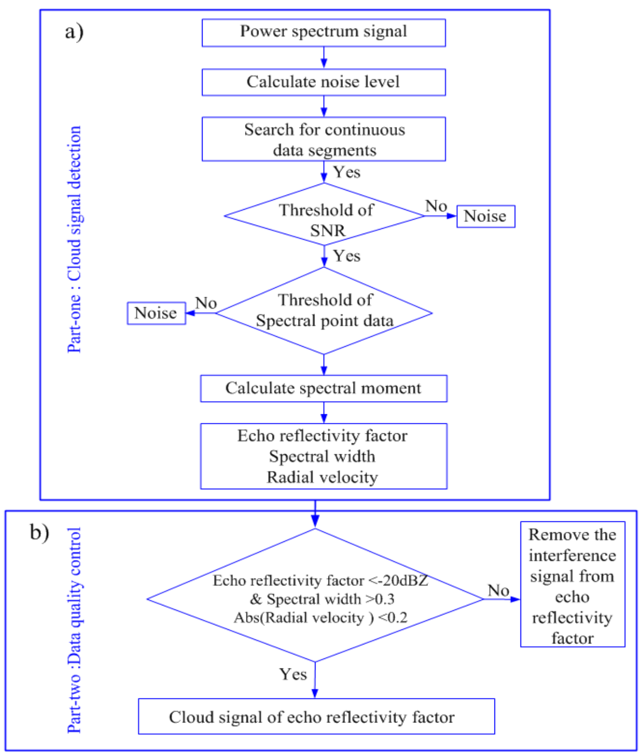

Fig. 6 Flow chart of MMCR cloud boundary detection

https://doi.org/10.5194/amt-2022-86
Preprint. Discussion started: 3 May 2022

According to the algorithm flow of Fig. 6, the power spectrum data at 22:44:00 on June 8, 2021 are analyzed to obtain the meteorological signals of the MMCR reflectivity factor, radial velocity and velocity spectrum width, as shown in Fig. 7a)-c). The nonmeteorological signals at the bottom (0~2 km) are effectively eliminated by using the quality control algorithm shown in Fig. 6b). The cloud signal shown in Fig. 7d) realizes the accurate detection of the cloud boundary.

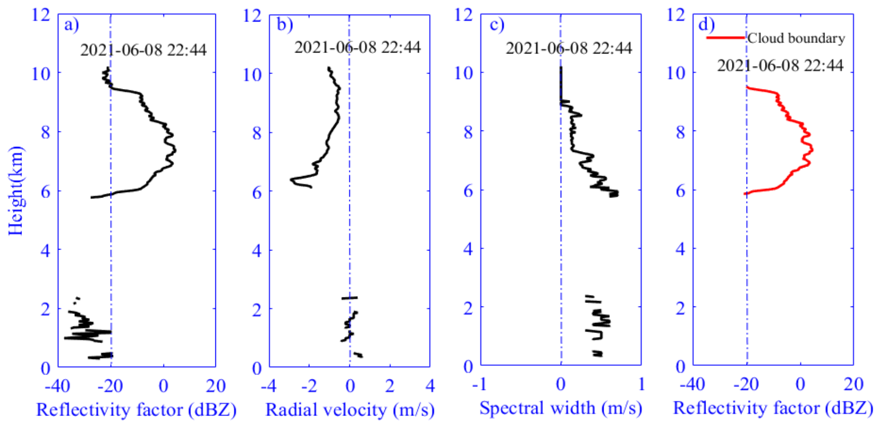

Fig. 7 Meteorological signals of MMCR at 22:44 on June 8, 2021. a) echo emissivity factor, b) radial velocity, c) velocity spectrum width, d) reflectivity factor after quality control

4 Results and discussion

4.1 Joint observation and analysis of various types of clouds

Clouds are rapidly changing (Veselovskii et al., 2017). They often appear in the form of single-layer clouds, multilayer clouds and precipitating clouds. Section 4 mainly uses the data inversion method proposed in Section 3 to analyze the changing characteristics of clouds under different conditions to obtain reliable cloud macro information. Although the spatial and temporal resolutions of the two detection devices are different, their close proximity allows a good 'point-to-point' quantitative comparison between the lidar and MMCR. Before data comparison and analysis, the low spatial resolution of MMCR and the low temporal resolution of the lidar are interpolated to keep the spatial and temporal resolutions of the two consistent (the time resolution is 5 s, and the spatial resolution is 3.75 m).

1) Case one studies of a single layer cloud

Clouds in the sky often appear as single-layer clouds, and the inversion of macroscopic parameters is simpler than that of multilayer clouds. June 08-09, 2021 (19:00~06:00), the lidar and MMCR jointly monitored the appearance of monolayer clouds in Xi'an. According to the data method described in Section 3.1, the SNR of P_{new_sf} and P_{new_sp} of the echo signal of the lidar @1064 nm are obtained time-height-indicator information (THI) and are shown in Figs. 8a) and 8b). The inversion results show that the thickness of the cloud layer is approximately 2 km, and the height of the cloud bottom decreases from 8 km to 4 km with the passage of observation time. After 05:00, the cloud layer developed deeper, and the laser beam penetrated 0.1 km into the cloud layer and was quickly attenuated.

https://doi.org/10.5194/amt-2022-86
Preprint. Discussion started: 3 May 2022

Rainfall begins at 06:00, and the lidar cannot continue effective observation and ends the experiment. The SNR in Fig. 8a) causes the SNR of the bottom signal to be large (0~2 km, and the echo signal within the range is not considered in the following cases). The cloud signals have higher SNR than the aerosol and background noise. P_{new_sp} highlights the **c**loud information from the aerosol signal and background noise and displays the details of the instability of the laser energy from 23:00 to 00:30 in Fig. 8b). Combined with the thresholds of SNR and P_{new_sp} of the cloud signal in Fig. 8a) and Fig. 8b), the cloud layer signal detected from the echo signal is shown in Fig. 8c).

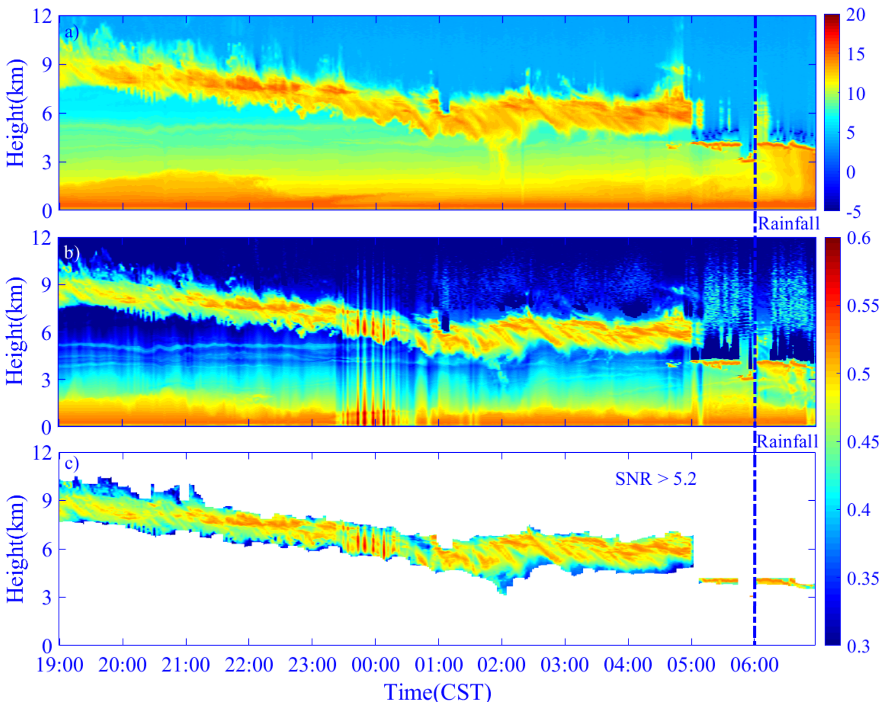

Fig. 8 The THI of the echo signal of the lidar @1064 nm from June 08 to 09, 2021. a) SNR of P_{new_sf}, b) P_{new_sp} of the 1064 nm signal, c) cloud information detection results (dotted line indicates rainfall time)

Figure 9 shows the cloud echo reflectivity factor of the MMCR at the same observation time period, and the cloud signals observed by the two devices have good macrostructural similarity before 06:00. As shown in Fig. 9a), when the quality control of the echo reflectance factor is not carried out, there are obvious nonmeteorological signals in the range of 0~2 km, and there are also some interference signals around the cloud. If we directly detect the cloud boundary with the echo reflectance factor in Fig. 9a), it will inevitably lead to the underestimation or overestimation of the cloud boundary. We can effectively eliminate the nonmeteorological signals at the bottom atmosphere and the interference signals around the clouds by using data quality control for the echo reflectivity coefficient in Fig. 9b). From the THI of the echo reflectivity of the cloud, the cloud layer starts at 03:00 and gradually develops from 7 km to 12 km (the lidar signal fails to show this detail). When rain appeared at 06:00, the cloud bottom boundary detected by the MMCR became blurred, but lidar could detect effectively (the cloud bottom boundary was ~3.8 km). In this case, we can apply lidar and MMCR to detect cloud bottom and cloud top boundaries, respectively, to achieve high-precision detection of cloud boundaries.

https://doi.org/10.5194/amt-2022-86
Preprint. Discussion started: 3 May 2022

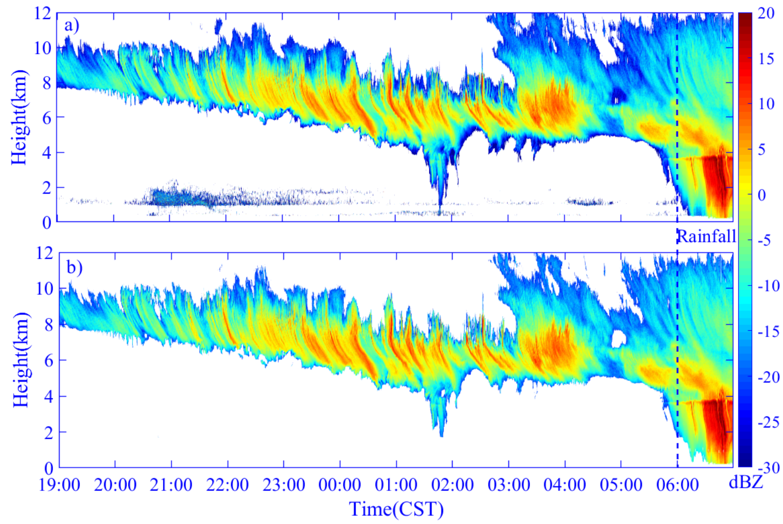

Fig. 9 The THI of echo reflectivity factor of MMCR from June 08 to 09, 2021. a) echo emissivity factor without quality control, b) echo reflectivity factor with quality control

The cloud boundary is retrieved from the cloud signals detected by the lidar and MMCR (Fig. 8c and Fig. 9 b), and the results are shown in Fig. 10. Between 19:00 and 05:00, the cloud bottom boundary height distribution retrieved by the two instruments is agreement. During the period of 21:00~06:00, with the deeper development of clouds, the MMCR can detect more cloud information than the lidar, especially from 03:00 to 06:00. Although lidar cannot penetrate more clouds in this period, it can obtain an effective cloud bottom boundary.

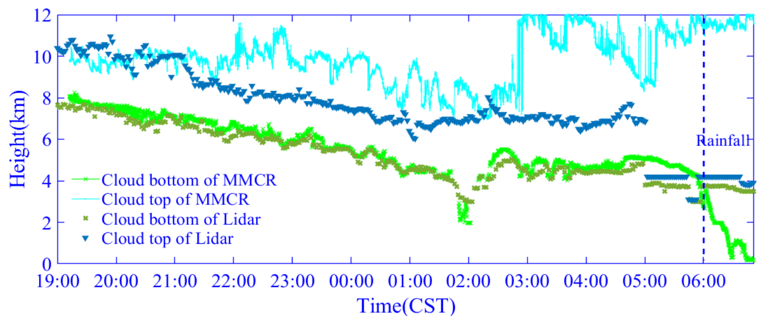

Fig. 10 Cloud boundary detected by lidar and MMCR from June 08 to 09, 2021

2) Case two studies of double-layer clouds

From March 4 to 5, 2021, the MMCR and lidar conducted joint observations, with a total observation time of 23 hours. By inverting the echo signal of the lidar @1064 nm, we obtained P_{new_sp} of the echo signal and the SNR of P_{new_sf}, and the plotted THIs are shown in Fig. 11a) and Fig. 1b). These THIs display that double layers of clouds appeared in the sky during the observation process. The low-level cloud is located at a height of 4 km, and its thickness is approximately 2 km, the high-level cloud lies at 7 km and its thickness is ~2.7 km. The SNR of the low-level cloud is significantly stronger than that of the high-level cloud, as shown in Fig. 11a. From the characteristic distribution of the P_{new_sp} signal in Fig. 11b), the low-level cloud rained from 18:30 to 18:45, and the

https://doi.org/10.5194/amt-2022-86
Preprint. Discussion started: 3 May 2022

cloud bottom height decreased sharply from 4 km to 0.6 km. Subsequently, the cloud layer gradually dissipated from 2 km to 0.05 km, and the dispersal that occurred from 02:00 to 10:00 was too strong for the lidar to detect more detailed information about the low-altitude cloud. We also notice the high-level cloud change characteristics shown in Fig. 11b). During the period from 17:00 to 01:00, there is a relatively weak P_{new_sp} signal in the height range between 7 km and 10 km. This indicates that the high-level cloud may be in the formation stage at this time, and the particle diameter and number concentration of clouds are so small that the lidar can only receive a very weak echo signal. As the observation progresses, the development of high-level clouds is relatively mature, and the structure is relatively stable from 01:00 to 15:00 (except 13:00). Combined with the thresholds of the SNR and intensity information of the cloud signal in Fig. 11a) and Fig. 11b), complete cloud signal detection can be realized, as shown in Fig. 11c).

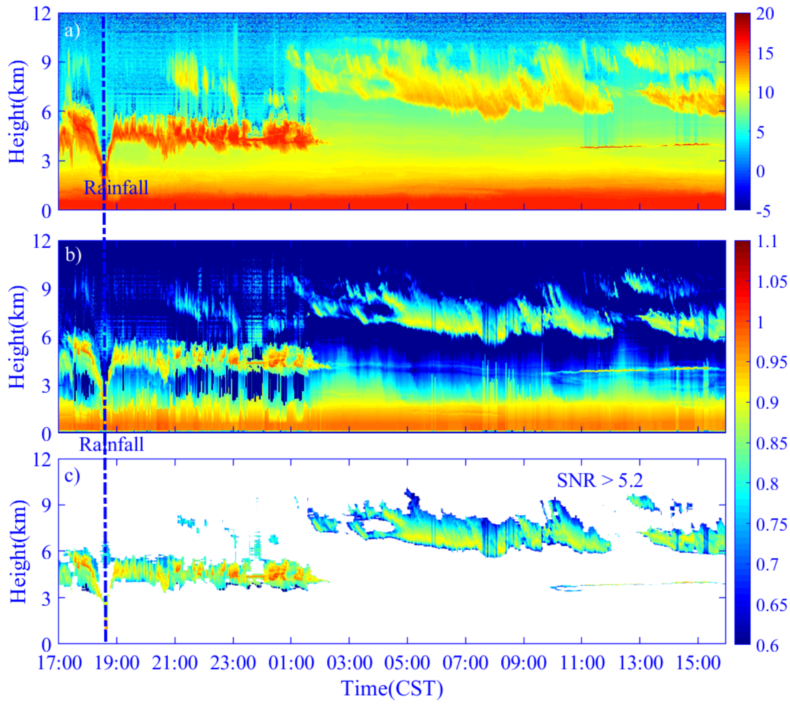

Fig. 11 The THI of the echo signal of the lidar @1064 nm from March 4 to 5, 2021. a) SNR of P_{new_sf}, b) P_{new_sp} of the 1064 nm signal, c) cloud information detection results (dotted line indicates rainfall time)

During the lidar observations, the MMCR also observed double clouds. Figs. 12a) and 12b) show the signal distribution characteristics of the echo reflectivity of MMCR without quality control and after quality control, respectively. It can be seen that in Fig. 12b), after data quality control, the nonmeteorological signals and interference signals at the bottom are effectively eliminated. From the joint observation results of the lidar and MMCR, it can be seen that the appearance and shape of clouds observed by the two are similar, and the occurrence of rainfall is monitored from 18:30 to 18:45. During the period from 15:00 to 01:00, the penetration ability of the MMCR is obviously better than that of the lidar, and more high-level cloud information is obtained. However, between 01:00 and 04:00 at high-level clouds (approximately 8 km), the MMCR detected only part of the debris cloud echo signal, while the lidar detected more cloud information. We can speculate that the main reason is that

https://doi.org/10.5194/amt-2022-86
Preprint. Discussion started: 3 May 2022

clouds were in the growth stage during this time period, their particle diameters were small or their concentrations were low. The echo signal of the MMCR is proportional to the 6th power of the particle diameter, while the echo signal of the lidar is proportional to the 2nd power of the particle diameter, so the lidar can detect clouds that the MMCR cannot detect. From 10:00 to 15:00, the MMCR also failed to detect the thin cloud signal at the lower layer (a height of approximately 4 km). Another reason for MMCR failing to detect thin clouds may also be that the spatial resolution is lower than that of lidar, which makes it unable to detect thin clouds.

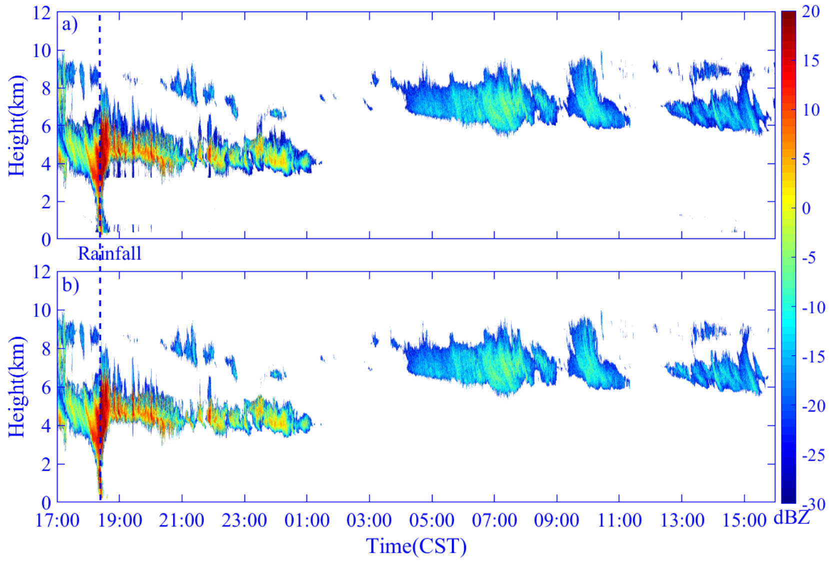

Fig. 12 The THI of echo reflectivity factor of MMCR from March 4 to 5, 2021, a) Echo emissivity factor without quality control, b) Echo reflectivity factor with quality control

Based on the cloud signals (Fig. 11c and Fig. 12b) jointly observed by the lidar and MMCR, the height distribution of the double-layer cloud boundaries is detected, as shown in Fig. 13. From the cloud boundary height distribution, it can be seen that the cloud boundary height distribution detected by the lidar and MMCR is relatively consistent for low-level clouds. For high-level clouds, the height of the cloud bottom boundary detected by the two instruments is similar, and the cloud top boundary detected by MMCR is higher than that detected by lidar. However, compared with MMCR, lidar has total supremacy in detecting the information of thin clouds.

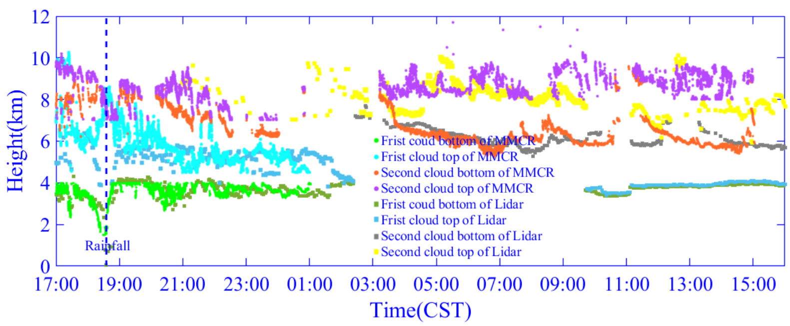

Fig. 13 Cloud boundary detected by the lidar and MMCR from March 4 to 5, 2021

https://doi.org/10.5194/amt-2022-86
Preprint. Discussion started: 3 May 2022

3) Case three studies of precipitating cloud

On March 10, 2021, the lidar and MMCR jointly observed the clouds before rainfall for 6 hours (06:00~11:00, and began to rain at 10:45). Fig. 14a) is the distribution of the SNR of P_{new_sf} with time and space, Fig. 14b) lays out the THI of P_{new_sp} of the @1064 nm echo signal, and Fig. 14c) shows the cloud signal detected by the thresholds of the SNR and P_{new_sp}. We inverted the echo reflectivity factor of MMCR and performed data quality control operations on them. The results are shown in Fig. 14d) and Fig. 14e), which are the echo reflections of MMCR without quality control and quality control, respectively. From the comparison, it is obvious that the data quality control can eliminate the interference signal very well, which makes the process of merging the high-level convective cloud and the low-level stratiform cloud clearer.

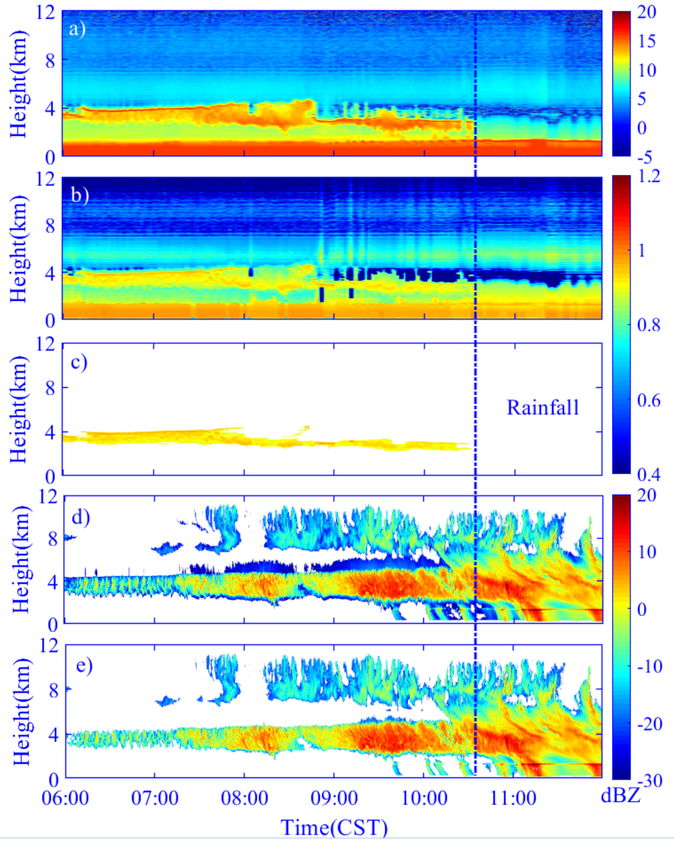

Fig. 14 The THI of echo signal of the lidar and MMCR on March 10, 2021. a) SNR of the 1064 nm signal, b) P_{new_sp} of the 1064 nm signal, c) cloud information detection results of the lidar, d) echo emissivity factor of the MMCR without quality control, e) echo reflectivity factor of the MMCR with quality control (dotted line indicates rainfall time)

By comparing the cloud information detected by the lidar and MMCR (in Fig. 14c) and Fig. 14e)), we can see that during the period from 06:00 to 10:00, the energy of the lidar beam is seriously attenuated at a height of approximately 4 km, resulting in a very weak echo signal and SNR above 4 km. As the observation time progresses, the phenomenon of rain storage (>15 dBZ) occurs in the cloud (Ellis et al., 2011; Williams et al., 2014). The severe attenuation of the lidar in the cloud leads to a sharp decrease in its detection ability, while the millimeter wave still

https://doi.org/10.5194/amt-2022-86
Preprint. Discussion started: 3 May 2022

Atmospheric Measurement Techniques
Discussions

has a strong penetrating ability. When rainfall occurs (at 10:45), neither the lidar nor MMCR can effectively identify the cloud bottom boundary, but MMCR can still detect the cloud top boundary information. The height distributions of cloud boundaries detected by lidar and MMCR are shown in Fig. 15. The height distribution of the cloud bottom and cloud top boundary detected by the two instruments is almost the same from 06:00 to 09:00 (the cloud bottom boundary is approximately 3 km, and the cloud top boundary is approximately 4.1 km). There was a drizzle falling from 09:00 to 10:45, and the lidar obtained an effective cloud bottom boundary. The boundary of the high-level convective cloud at ~8 km and the deep cloud layer from 10:45 to the end of observation can only be detected by MMCR.

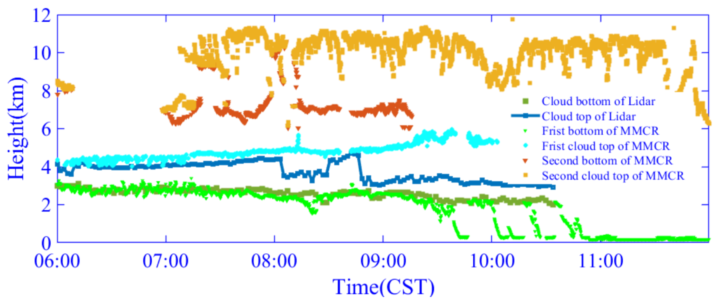

Fig. 15 Cloud boundary detected by the lidar and MMCR on March 10, 2021

From the differences in the height distribution of the cloud boundaries reached by the two devices in the above three different situations, it can be seen that when a single layer of stratiform clouds appears in the sky, the heights of the cloud bottom boundary detected by MMCR and lidar are approximately the same. When there are multilayer clouds, MMCR and lidar have good consistency in the detection results of the cloud bottom boundary height of the low-level cloud, but the energy of the lidar beam of attenuates seriously in the low-level cloud, resulting in the inability to fully obtain the effective bottom boundary of low-level clouds and the height boundary of high-level clouds. In this case, MMCR can obtain more complete height information of the multilayer cloud boundary. Usually, the closer to rainfall, the deeper the cloud layer develops, the beam of the lidar will be seriously attenuated, and more cloud information cannot be obtained. In other words, MMCR still has the ability to penetrate the cloud layer and detect the complete cloud information at this time. Therefore, the joint observation of the lidar and MMCR can comprehensively identify and detect cloud boundary conditions in detail. The difference between the cloud boundaries detected by the two may also be due to the different scattering mechanisms of cloud particles to millimeter-wave electromagnetic waves and laser beams or the difference in the methods used by the two devices to determine the cloud boundary, so that there are some differences in the cloud boundary height results.

4.2 Statistics and analysis of cloud boundary distribution characteristics in Xi'an

In 2021, the Lidar and MMCR radar conducted cloud observation experiments at the Jinghe meteorological station, in which the MMCR accumulated 302 days of data (7248 hours in total) and the lidar observed 126 days (872.5 hours in total). Due to some unavoidable external reasons, the lidar failed to carry out the observation experiment at the same time as the MMCR. To further analyze the changes in the height distribution of cloud boundaries in Xi'an in 2021, we plan to employ MMCR data to replace the data of periods when the lidar is not running. Accordingly, it is necessary to analyze the correlation of the cloud bottom boundary height detected by the

https://doi.org/10.5194/amt-2022-86
Preprint. Discussion started: 3 May 2022

two devices. We randomly select 80 hours of data in the joint observation period (avoid the rainfall period) and calculate the cloud boundary detection results of the lidar and MMCR according to the data processing methods in sections 3.1 and 3.2. As shown in Fig. 16, when the quality control of the MMCR is performed, the correlation between the detected cloud boundary and the lidar detection result is increased from 0.627 (in Fig. 16a)) to 0.803 (in Fig. 16b)). Moreover, under the premise that the difference in cloud boundaries caused by the different detection principles and detection algorithms of the two devices cannot be avoided, we can use the cloud boundary data detected by MMCR to replace the missing lidar data.

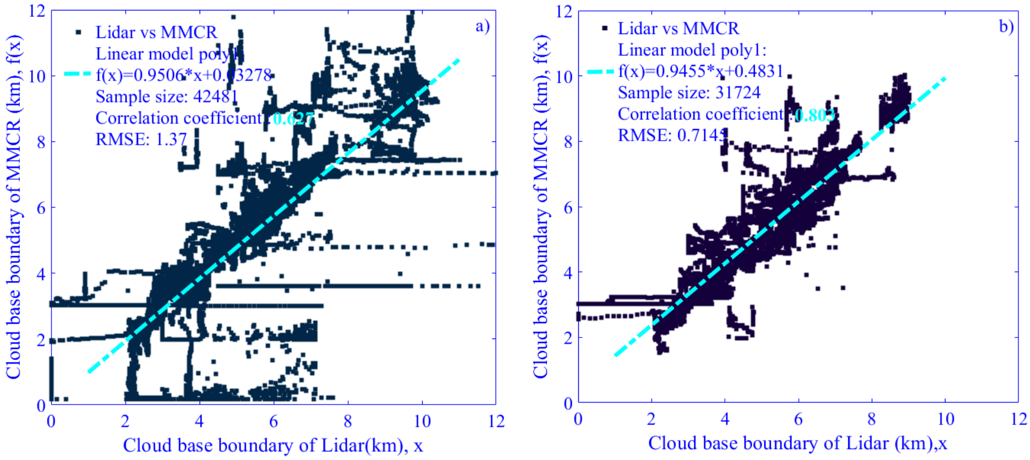

Fig. 16 Correlation between lidar and MMCR cloud bottom boundary. a) without quality control; b) with quality control)

From the above three cloud observation cases, it can be seen that MMCR has more advantages than lidar in detecting cloud top boundaries. Therefore, when calculating the cloud boundary height distribution characteristics over Xi'an in 2021, we only count the cloud top boundary height detected by MMCR and take it as the actual cloud top boundary. The statistical rules shown in Table 3 are established for the statistics of cloud bottom boundary information. The experimental data of 302 days (65 days in spring (January-March), 84 days in summer (April-June), 65 days in autumn (July-September) and 88 days in winter (October-December) observed in 2021 are classified and sorted out to ease the statistics and analysis of the variation characteristics of cloud boundary height.

Table 3 Statistical rules of cloud bottom boundary information

Detection equipment	Observation	Detection conditions	Record cloud bottom boundary
Both the lidar and MMCR	Case 1	Thin cloud: the lidar detects bottom; MMCR did not detect the cloud bottom	Results of the lidar
	Case 2	Drizzle: the lidar detects bottom; bottom of MMCR is blurred	Results of the lidar
	Case 3	Both the lidar and MMCR detect cloud bottom	Record the lower value of the cloud base boundary
MMCR	Case 4	MMCR detected cloud bottom	Results of MMCR
	Case 5	Drizzle: bottom of MMCR is blurred	No results are recorded

https://doi.org/10.5194/amt-2022-86
Preprint. Discussion started: 3 May 2022

Atmospheric Measurement Techniques Discussions

This study defines "cloud occurrence frequency" as the ratio of cloud occurrence times to total detection times during the analyzed period. It is observed that the total sample size is N, and the sample size of cloud boundaries appearing at different height levels (altitude range from 1.5 km to 12 km is divided into 50 levels) is n_i. The seasonal distribution characteristics of the cloud boundary height are calculated according to Eq. (7),

$$y_{\_cloud} = \frac{n_i}{N}(n_i \in N, \mathrm{i} = 1....50) \qquad (7)$$

Fig. 17 shows that the cloud top boundary occurrence frequency in spring and summer presents a bimodal distribution. In spring, the height of the first peak lies approximately 1.5 ~ 1.9 km, and the second peak is 7.8 ~ 8 km. The heights of the first and second peaks are approximately 1.5 ~ 3 km and 8 ~ 12 km, respectively, in summer. In autumn and winter, the frequency of cloud top boundary heights above 2 km is almost in the range of 0.3 to 0.4. For the vertical distribution characteristics of the cloud bottom boundary, there is a triple-mode pattern in four seasons. The frequency distribution characteristics of the cloud bottom boundary height in spring and summer are relatively similar. The first most obvious narrow peak < 1.5 km is the frequency change caused by boundary layer clouds, the second narrow peak is located at 3 ~ 4 km, and the third peaks in spring and summer are located at 6 ~ 8 km and 7 ~ 9 km, respectively. From the distribution characteristics of the cloud bottom boundary in summer and spring, it can be guessed that convective and cirrus clouds may be dominant in these two seasons. The frequency distribution of clouds above 8 km in autumn is the largest in the four seasons, and we can speculate that stratus clouds and cumulus clouds are mainly in this season. In winter, the height range of clouds is narrow, and the numerical range is wide, which may be mainly stratiform clouds. This is consistent with the analysis results of Zhao et al. (Zhao et al., 2014) at the SGP site and Hailing Xie (Xie et al., 20217) at the SACOL site. Although there are some differences in the cloud boundary frequency distribution at some heights, the overall change trend is roughly the same.

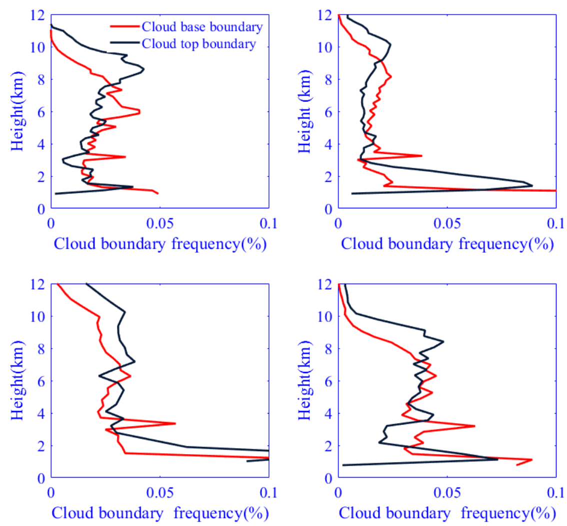

Fig. 17 Frequency distribution of cloud boundaries during (a) spring, (b) summer, (c) autumn and (d) winter from January to December 2021 at Xi'an Jinghe National Meteorological Station

Fig. 18a) shows the monthly variation frequency distribution of clouds. The months with the largest (96%) and smallest (42%) cloud occurrence frequencies are August and December, respectively. Almost more than 34% of the clouds appear in the form of single layer clouds every month. Compared with January, February, November and December, the frequencies of double-layer clouds, triple-layer clouds and more clouds in other months are higher. It is also possible that there are some thin clouds and broken clouds in the upper layer, which are summarized as multilayer clouds by the algorithm. As shown in Fig. 18b), the normalized monthly distribution of cloud amount shows that the minimum cloud amount is 0.65 in spring and the maximum is 2.46 in summer, indicating that warm atmospheric conditions are more conducive to the formation and development of clouds.

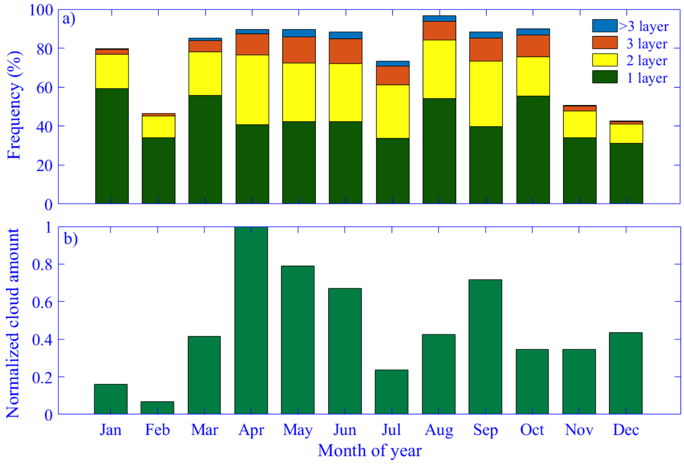

Fig. 18 The monthly variation in cloud frequency distribution and cloud amount in 2021 a) monthly variation in the frequency of the number of cloud layers. b) monthly variation in cloud amount

Fig. 19 shows the frequency change characteristics of the cloud boundary vertical height distribution in 2021, in which the frequency of the cloud bottom boundary below the vertical height of 1.5 km is greater than 10%, the frequency within the height range of 3.06 km and 3.6 km is approximately 3.24%, and the frequency above 8 km is less than 2%. The frequency of the cloud top boundary at vertical heights has a bimodal distribution; the first narrow peak is located at 1.5~3.1 km, and the second peak lies at approximately 7.5~10.5 km. Combined with the changing characteristics of cloud layers, it can be seen that during the observation process in Xi'an in 2021, the frequency of stratiform clouds below 3.5 km is the largest, and the frequency of high-level ice clouds or cirrus clouds above 8 km is small.

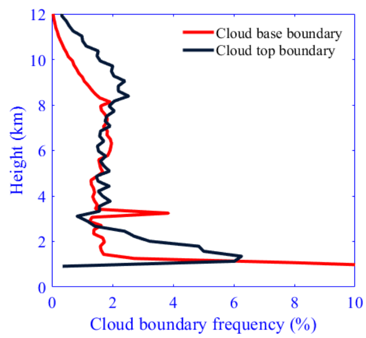

Fig. 19 Frequency distribution of cloud boundaries at vertical heights at Xi'an Jinghe National Meteorological Station in 2021

https://doi.org/10.5194/amt-2022-86
Preprint. Discussion started: 3 May 2022

5 Conclusions

Based on the detection principle of lidar and MMCR, this study realizes the accurate recognition of cloud signals from aerosols and background noise signals by enhancing the lidar echo signal and combining its SNR change. The $SNR_{\min}$ and spectral point continuous threshold are used to identify the cloud signal in the power spectrum of the MMCR, and data quality control technology is implemented for the echo reflectivity factor, which eliminates the interference of nonmeteorological signals on the cloud signal and improves the accuracy of cloud boundary detection.

The case analysis results of the joint lidar and MMCR observations show that the two devices have their own advantages in detecting cloud boundaries. 1) For the development of deep clouds, the lidar beam will be seriously attenuated and cannot penetrate the clouds, while the MMCR can penetrate more clouds and obtain the real cloud top boundary. 2) In detecting low-level clouds, the echo reflectivity of MMCR is easy for ground-based clutter interference, and the echo signals observed by lidar can help eliminate clutter to obtain accurate cloud bottom boundaries. 3) When precipitation occurs (except for heavy precipitation), it is difficult to distinguish the cloud bottom height from the echo reflectivity factor of the MMCR, while lidar can reverse the effective cloud bottom boundary to a certain extent. 4) For thin clouds, lidar can obtain more complete information than MMCR. Therefore, when employing the lidar and MMCR to jointly observe the cloud boundary, their respective strengths can be exerted, and their shortcomings can be compensated for each other, making the detection of cloud boundary height more detailed and accurate.

Based on the statistical analysis of the changes and distribution of cloud boundaries in Xi'an in 2021, it can be seen that more than 34% of the clouds appear in the form of a single layer of every month. The cloud amount is the lowest in spring and the highest in summer. The seasonal variation in cloud boundary height shows that the distribution characteristics of cloud boundaries in spring and summer are similar, and the frequency of high-level clouds in the range of 8 ~ 10 km is greater than that in the other two seasons. The stratiform clouds appearing below 3.5 km in autumn have the highest frequency, and the high-level ice clouds or cirrus clouds above 8 km in winter are less likely to appear. In this paper, by retrieving the cloud data observed by the lidar and MMCR in 2021, the results of the cloud boundary detected by the two instruments are analyzed and compared to determine the advantages and limitations of the lidar and MMCR in cloud boundary detection, which can provide more information for understanding and studying aerosol-cloud interactions, climate change and forecasting numerical models in Xi'an.

Data availability

Data and code related to this article are available upon request to the corresponding author.

Author contributions

In this paper, Yun Yuan proposed new methods and theories, processed and analyzed the data in the paper, and wrote the manuscript. Huige Di made many revisions and guidance to the manuscript, and put forward many feasible suggestions. Tao Yang collected the experimental data and maintained the equipment. Yuanyuan Liu sorted and classified the original experimental data. Qimeng Li calibrated the experimental system. Qing Yan coordinated the placement and calibration of experimental equipment. Dengxin Hua led the project, instrument development, experimental design and data analysis.

Competing interests

The authors declare that they have no conflicts of interest related to this work.

Financial support

This research was supported by the National Natural Science Foundation of China (NSFC): 61875163 and 42130612.

References

Apituley A, van Lammeren A, Russchenberg H.: High time resolution cloud measurements with lidar during CLARA, Physics & Chemistry of the Earth Part B Hydrology Oceans & Atmosphere, 25(2), 107-113, doi: 10.1016/S1464-1909(99)00135-5, 2000.

Brown P R A, Illingworth A J, Heymsfield A J, Mcfarquhar G M, Browning K A, Gosset M.: The role of spaceborne millimetre-wave radar in the global monitoring of ice cloud, J Appl Meteor, 34, 2346-2366, doi:10.1049/ic:19950202, 1995.

Cao X, Lu G, Li M, et al.: Statistical Characteristics of Cloud Heights over Lanzhou, China from Multiple Years of Micro-Pulse Lidar Observation, Atmosphere-Basel, 12(11), 1415, doi: 10.3390/atmos12111415, 2021.

Clothiaux E E, Moran K P, Martner B E, et al.: The atmospheric radiation measurement program cloud radars: Operational modes, J Atmos Ocean Tech, 16(7), 819-827, doi: 10.1175/1520-0426(1999)016<0819:tarmpc>2.0.co;2, 1999.

Cordoba-Jabonero C, Lopes F J S, Landulfo E, et al.: Diversity on subtropical and polar cirrus clouds properties as derived from both ground-based lidars and CALIPSO/CALIOP measurements, Atmos Res, 183, 151-165, doi:10.1016/j.atmosres.2016.08.015, 2017.

Ellis S M, Vivekanandan J.: Liquid water content estimates using simultaneous S and K a band radar measurements, Radio Sci, 46(02), 1-15, doi:10.1029/2010RS004361, 2011.

Görsdorf U, Lehmann V, Bauer-Pfundstein M, et al.: A 35-GHz polarimetric Doppler radar for long-term observations of cloud parameters—Description of system and data processing, J Atmos Ocean Tech, 32(4), 675-690, doi:10.1175/JTECH-D-14-00066.1, 2015.

Görsdorf U, Lehmann V, Bauer-Pfundstein M, et al.: A 35-GHz polarimetric Doppler radar for long-term observations of cloud parameters—Description of system and data processing, J Atmos Ocean Tech, 32(4), 675-690. doi:10.1175/JTECH-D-14-00066.1, 2015.

Haper W G.: Examples of cloud detection with 8.6-millimeter radar (radar resolution capability for cloud detection), Meteor Mag, 95, 106-122, 1966.

Hobbs P V, Funk N T, Weiss Sr R R, et al.: Evaluation of a 35 GHz radar for cloud physics research, J Atmos Ocean Tech, 2(1), 35-48, doi:10.1175/1520-0426(1985)002<0035:EOAGRF>2.0.CO;2, 1985.

Intrieri J M, Stephens G L, Eberhard W L, et al.: A method for determining cirrus cloud particle sizes using lidar and radar backscatter technique, J Appl Meteorol Clim, 32(6), 1074-1082, doi:10.1175/1520-0450(1993)0322.0.CO;2, 1993.

Kitova N S, Ivanova K, Mikhalev M A, et al.: Statistical investigation of cloud base height time evolution, Proceedings of SPIE - The International Society for Optical Engineering, 5226, 280-284, doi: 10.1117/12.519500, 2003.

Kollias P, Clothiaux E E, Miller M A, et al.: Millimeter-wavelength radars: New frontier in atmospheric cloud and precipitation research, B Am Meteorol Soc, 88(10), 1608-1624, doi: 10.1175/BAMS-88-10-1608, 2017.

Kollias P, Miller M A, Luke E P, et al.: The Atmospheric Radiation Measurement Program cloud profiling radars: Second-generation sampling strategies, processing, and cloud data products, J Atmos Ocean Tech, 24(7), 1199-1214, doi:10.1175/JTECH2033.1, 2007.

Kovalev V A, Newton J, Wold C, et al.: Simple algorithm to determine the near-edge smoke boundaries with scanning lidar, Appl Optics, 44(9), 1761-1768, doi:10.1364/ao.44.001761, 2005.

Kuji M.: Retrieval of water cloud top and bottom heights and the validation with ground-based observations, Proceedings of SPIE - The International Society for Optical Engineering, 8890, 223-228, doi: 10.1117/12.2029169. 2013.

Li J M, Yi Y H, Stamnes K, et al.: A new approach to retrieve cloud base height of marine boundary layer clouds, Geophys Res Lett, 40(16), 4448-4453, doi:10.1002/grl.50836, 2013.

Lohmann U, Gasparini B.: A cirrus cloud climate dial?, Science, 357(6348), 248-249, doi:10.1126/science.aan3325, 2017.

Luke E P, Kollias P, Johnson K L, et al.: A technique for the automatic detection of insect clutter in cloud radar returns, J Atmos Ocean Tech, 25(9), 1498-1513, doi:10.1175/2007JTECHA953.1, 2008.

Mao F, Gong W, Zhu Z.: Simple multiscale algorithm for layer detection with lidar, Appl Optics, 50(36), 6591-6598, doi:10.1364/AO.50.006591, 2011.

Melnikov V M, Istok M J, Westbrook J K.: Asymmetric radar echo patterns from insects, J Atmos Ocean Tech, 32(4), 659-674, doi:10.1175/JTECH-D-13-00247.1, 2015.

Melnikov V, Leskinen M, Koistinen J.: Doppler velocities at orthogonal polarizations in radar echoes from insects and birds, IEEE Geosci Remote S, 11(3), 592-596, doi:10.1109/LGRS.2013.2272011, 2013.

Morille Y, Haeffelin M, Drobinski P, et al.: STRAT: An automated algorithm to retrieve the vertical structure of the atmosphere from single-channel lidar data, J Atmos Ocean Tech, 24(5), 761-775, doi:10.1175/JTECH2008.1, 2007.

Motty G S, Satyanarayana M, Jayeshlal G S, et al.: Lidar observed structural characteristics of higher altitude cirrus clouds over a tropical site in Indian subcontinent region, J Atmos Sol-Terr Phy, 179, 367-377, doi: 10.1016/j.jastp.2018.08.013, 2018.

Motty G S, Satyanarayana M, Jayeshlal G S, et al.: Lidar observed structural characteristics of higher altitude cirrus clouds over a tropical site in Indian subcontinent region, J Atmos Sol-Terr Phy, 179, 367-377, doi: 10.1016/j.jastp.2018.08.013, 2018.

Nakajima T, King M D, Spinhirne J D.: Determination of the Optical Thickness and Effective Particle Radius of Clouds from Reflected Solar Radiation Measurements Part I: Theory, Nature, 517(7536), 41.e1–41.e21, doi: 10.1038/517529a, 1991.

Oh S B, Kim Y H, Kim K H, et al.: Verification and correction of cloud base and top height retrievals from Ka-band cloud radar in Boseong, Korea, Adv Atmos Sci, 33(1), 73-84, doi:CNKI:SUN:DQJZ.0.2016-01-007, 2016.

Pal S R, Steinbrecht W, Carswell A I.: Automated method for lidar determination of cloud-base height and vertical extent, Appl Optics, 31(10), 1488-1494, doi:10.1364/AO.31.001488, 1992.

https://doi.org/10.5194/amt-2022-86
Preprint. Discussion started: 3 May 2022

Platt C M, Young S A, Carswell A I, et al.: The experimental cloud lidar pilot study (ECLIPS) for cloud–radiation research, B Am Meteorol Soc, 75(9), 1635-1654, doi:10.1175/1520-0477(1994)075<1635:TECLPS>2.0.CO;2, 1994.

Riddle AC, Gage KS, Balsley BB, Ecklund WL, Carter DA.: Poker Flat MST Radar Data Bases, NOAA Tech, Memorandum, ERL AL-11, 1989.

Sassen K, Mace G.: Ground-based Remote Sensing of Cirrus Clouds, Oxford University Press, 168–196, 2001.

Sauvageot H.: Retrieval of vertical profiles of liquid water and ice content in mixed clouds from Doppler radar and microwave radiometer measurements, J Appl Meteorol Clim, 35(1), 14-23, doi:10.1175/1520-0450(1996)0352.0.CO;2, 1996.

Sherwood S C, Bony S, Dufresne J L.: Spread in model climate sensitivity traced to atmospheric convective mixing, Nature, 505(7481), 37-42, doi: 10. 1038/nature12829, 2014.

Shupe M D, Kollias P, Matrosov S Y, et al.: Deriving mixed-phase cloud properties from Doppler radar spectra, J Atmos Ocean Tech, 21(4), 660-670, doi:10.1175/1520-0426(2004)0212.0.CO;2, 2004.

Stephens G L, Li J, Wild M, et al.: An update on Earth's energy balance in light of the latest global observations, Nat Geosci, 5(10), 691-696, doi: 10.1038/ngeo1580, 2012.

Stephens, Graeme L.: Cloud Feedbacks in the Climate System: A Critical Review, J Climate, 18(2), 237-273, doi:10.1175/JCLI-3243.1, 2005.

Streicher J, Werner C, Koepp F.: Verification of lidar visibility, cloud base height, and vertical velocity measurements by laser remote sensing, SPIE, 2506, 576-579, 1995.

Thorsen T J, Fu Q, Comstock J M.: Cloud effects on radiative heating rate profiles over Darwin using ARM and A-train radar/lidar observations, J Geophys Res-Atmos, 118(11), 5637-5654, 2013.

Varikoden H, Harikumar R, Vishnu R, et al.: Observational study of cloud base height and its frequency over a tropical station, Thiruvananthapuram, using a ceilometer, Int J Remote Sens, 32(23), 8505-8518, doi: 10.1080/01431161.2010.542199, 2011.

Veselovskii I, Goloub P, Podvin T, et al.: Spectral dependence of backscattering coefficient of mixed phase clouds over West Africa measured with two-wavelength Raman polarization lidar: Features attributed to ice-crystals corner reflection, J Quant Spectrosc Ra, 202, 74-80, doi:10.1016/j.jqsrt.2017.07.028, 2017.

Wang J, Rossow W B.: Determination of cloud vertical structure from upper-air observations, J Appl Meteorol Clim, 34(10), 2243-2258, doi: 10.1175/15200450(1995)034%3C2243: DOCVSF%3E2.0.CO;2, 1995.

Wang J, Rossow W B.: Effects of cloud vertical structure on atmospheric circulation in the GISS GCM, J Climate, 11(11), 3010-3029, doi: 10.1175/1520-0442(1998)0112.0.CO;2, 1998.

Wang Z.: Cloud property retrieval using combined ground-based remote sensors, The University of Utah, 2000.

Ward J G, Merceret F J.: An automated cloud-edge detection algorithm using cloud physics and radar data, J Atmos Ocean Tech, 21(5), 762-765, doi:10.1175/1520-0426(2004)0212.0.CO;2, 2004.

Wild M.: New Directions: A facelift for the picture of the global energy balance, Atmos Environ, 55(none), 366-367, doi:10.1016/j.atmosenv.2012.03.022, 2012.

Williams C R, Bringi V N, Carey L D, et al.: Describing the shape of raindrop size distributions using uncorrelated raindrop mass spectrum parameters, J Appl Meteorol Clim, 53(5), 1282-1296, doi:10.1175/JAMC-D-13-076.1, 2014.

https://doi.org/10.5194/amt-2022-86
Preprint. Discussion started: 3 May 2022

Atmospheric Measurement Techniques Discussions

Xie H, Zhou T, Fu Q, et al.: Automated detection of cloud and aerosol features with SACOL micro-pulse lidar in northwest China, Opt Express, 25(24), 30732-30753, doi:10.1364/OE.25.030732, 2017.

Young S A.: Analysis of lidar backscatter profiles in optically thin clouds, Appl Optics, 34(30), 7019-7031, doi:10.1364/AO.34.007019, 1995.

Zcab C, Xs B.: Dynamic spatial fusion of cloud top phase from PARASOL, CALIPSO, cloudsat satellite data, J Quant Spectrosc Ra, 224, 176-184, doi:10.1016/j.jqsrt.2018.11.010, 2019.

Zhang J Q, Chen H B, Xia X A.: Dynamic and thermodynamic features of low and middle clouds derived from atmospheric radiation measurement program mobile facility radiosonde data at Shouxian, Adv Atmos Sci, 33(1), 21-33, doi:10. 1007/s00376-015-5032-8, 2012.

Zhang L, Dong X Q, Kennedy A.: Evaluation of NASA GISS post-CMIP5 single column model simulated clouds and precipitation using ARM Southern Great Plains observations, Adv Atmos Sci, 34(3), 306-320, doi:10.1007/s00376-016-5254-4, 2017.

Zhang Y, Zhang L, Guo J, et al.: Climatology of cloud-base height from long-term radiosonde measurements in China, Adv Atmos Sci, 35(2), 158-168, doi: 10.1007/s00376-017-7096-0, 2018.

Zhao C, Wang Y, Wang Q, et al.: A new cloud and aerosol layer detection method based on micropulse lidar measurements, J Geophys Res-Atmos, 119(11), 6788-6802, doi: 10.1002/2014JD021760, 2014.

Zheng J, Zhang J, Zhu K, et al.: Gust front statistical characteristics and automatic identification algorithm for CINRAD, J Meteorol Res-Prc, 28(4), 607-623, doi: 10.1007/s13351-014-3240-2, 2014.

Zhou C, Zelinka M D, Klein S A.: Impact of decadal cloud variations on the Earth's energy budget, Nat Geosci, 9(12), 871-874, doi: 10.1038/ngeo2828, 2016.

Zhou Q, Zhang Y, Li B.: Cloud-base and Cloud-top Heights Determined from a Ground-based Cloud Radar in Beijing, China, Atmos Environ, 201(MAR.), 381-390, doi:10.1016/j.atmosenv.2019.01.012,2019.